

Probabilistic and Semantic Descriptions of Image Manifolds and Their Applications

Peter Tu^{1,*}, Zhaoyuan Yang¹, Richard Hartley², Zhiwei Xu², Jing Zhang²,
Yiwei Fu¹, Dylan Campbell², Jaskirat Singh², and Tianyu Wang²

¹ *Computer Vision and Machine Learning Laboratory, General Electric Research, Niskayuna, New York, USA*

² *School of Computing, College of Engineering, Computing and Cybernetics, Australian National University, Canberra, Australia*

Correspondence*:

Corresponding Author: Peter Tu
tu@ge.com

ABSTRACT

This paper begins with a description of methods for estimating probability density functions for images that reflects the observation that such data is usually constrained to lie in restricted regions of the high-dimensional image space — not every pattern of pixels is an image. It is common to say that images lie on a lower-dimensional manifold in the high-dimensional space. However, although images may lie on such lower-dimensional manifolds, it is not the case that all points on the manifold have an equal probability of being images. Images are unevenly distributed on the manifold, and our task is to devise ways to model this distribution as a probability distribution. In pursuing this goal, we consider generative models that are popular in AI and computer vision community. For our purposes, generative/probabilistic models should have the properties of 1) sample generation: it should be possible to sample from this distribution according to the modelled density function, and 2) probability computation: given a previously unseen sample from the dataset of interest, one should be able to compute the probability of the sample, at least up to a normalising constant. To this end, we investigate the use of methods such as normalising flow and diffusion models. We then show that such probabilistic descriptions can be used to construct defences against adversarial attacks. In addition to describing the manifold in terms of density, we also consider how semantic interpretations can be used to describe points on the manifold. To this end, we consider an emergent language framework which makes use of variational encoders to produce a disentangled representation of points that reside on a given manifold. Trajectories between points on a manifold can then be described in terms of evolving semantic descriptions.

Keywords: image manifold, normalising flow, diffusion model, maximum likelihood estimation, adversarial attacks and defences, semantic disentanglement

1 INTRODUCTION

Understanding the complex probability distribution of the data is essential for image authenticity and quality analysis, but is challenging due to its high dimensionality and intricate domain variations (Pope et al., 2021; Gomtsyan et al., 2019). Seen images usually have high probabilities on a low-dimensional manifold embedded in the higher-dimensional space of the image encoder. On such a manifold, however, not every point can be decoded into a realistic image because of the unevenly distributed probabilities. Therefore, it is important to compute the probability in the latent space to indicate whether the corresponding image is in

a high-density region of the space (Hajri et al., 2017; Klein et al., 2022; Grover et al., 2018; Papamakarios et al., 2021; Chang et al., 2017; Alanis-Lobato et al., 2016; Coeurdoux et al., 2022). This helps to distinguish seen images from unseen images, or synthetic images from real images. Some works train a discriminator with positive (real) and negative (synthetic) examples in the manner of contrastive learning (Liu et al., 2022) or analyse their frequency differences (Wang et al., 2020). However, they do not address this problem using the probabilistic framework afforded by modern generative models.

In this work, we directly calculate the log-probability of an image by utilising generative models that assign high probabilities to seen images and low probabilities to unseen images. We use normalising flow (NF) (Rezende and Mohamed, 2016; Papamakarios et al., 2021) and diffusion models (Ho et al., 2020; Luo, 2022; Song et al., 2021) as image generators. NF models learn an image embedding space that conforms to a predefined distribution, usually a Gaussian. In contrast, diffusion models diffuse images with Gaussian noise in each forward step and learn denoising gradients for the backward steps. A random sample from the Gaussian distribution can then be analytically represented on an image manifold and visualised through an image decoder (for NF models) or denoiser (for diffusion models).

These samples can be thought of as being composed of several meaningful semantic attributes. It is often desirable that these attributes be orthogonal to each other in the sample latent space so as to achieve a controllable and interpretable representation. In this work, we evaluate their robustness to adversarial and patch attacks (Brown et al., 2017; Liu et al., 2020; Hwang et al., 2023; Xiang et al., 2021; Chou et al., 2019; Madry et al., 2018; Tramer et al., 2017; Carlini and Wagner, 2016) in image space and defend against the same using semantic consistency with a purification loss. We also disentangle their semantics in the latent space by using a variational autoencoder (VAE) (Kingma and Welling, 2013) in the framework of emergent languages (EL) (Havrylov and Titov, 2017; Mu et al., 2023; Tucker et al., 2021; Kubricht et al., 2020; Santamaria-Pang et al., 2020). This allows the latent representation to be more robust, interpretable, compositional, controllable, and transferable.

We organise this paper into three sections, each with their own experiments: log-likelihood estimation for a given image under normalising flow and diffusion models (see Section 2), adversarial attacks and defences in image space for preserving semantics (see Section 3), and semantic disentanglement in emergent languages for a latent representation of object attributes, using a proposed GridVAE model (see Section 4).

2 MAXIMUM LIKELIHOOD ESTIMATION WITH IMAGE GENERATORS

We evaluate the log-probability of a given image using 1) a hierarchical normalising flow model, 2) a diffusion model adapted to taking large sampling steps, and 3) a diffusion model that uses a higher-order solution to increase generation robustness.

2.1 Hierarchical Normalising Flow Models

Normalising flow (NF) refers to a sequence of invertible functions that may be used to transform a high-dimensional image space to a low-dimensional embedding space corresponding to a probability distribution, usually Gaussian. Dimensionality reduction is achieved via an autoencoding framework. For the hierarchical model, the latent vector corresponding to the image \mathbf{x}_i at each level i is computed as

$$\mathbf{z}_i = g_i(\mathbf{y}_i) = g_i \circ f_i(\mathbf{x}_i) \sim \mathcal{N}(\mathbf{0}, \mathbf{1}), \quad (1)$$

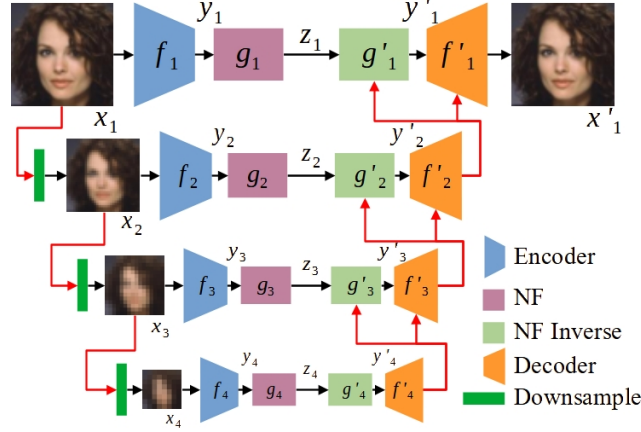


Figure 1. A 4-level hierarchical normalising flow model, where each level involves the functions (f_i, g_i, g'_i, f'_i) . The normalising flow (NF) model is based on Glow (Kingma and Dhariwal, 2018); the downsampling block decreases image resolution by a factor of two; and the output of each higher ($i > 1$) level is conditioned on the output of the lower level. We first train all autoencoders $\{f_i, f'_i\}$ jointly, then train all flows $\{g_i, g'_i\}$ jointly, to obtain the generated image \mathbf{x}'_1 . The latent variable \mathbf{z}_i conforms to the standard Gaussian distribution $\mathcal{N}(\mathbf{0}, \mathbf{1})$ during training; at test time, \mathbf{z}_i is sampled from $\mathcal{N}(\mathbf{0}, \mathbf{1})$ for image generation.

and the inversion of this process reconstructs the latent \mathbf{z}'_i to \mathbf{x}'_i as

$$\mathbf{x}'_i = f'_i \circ g'_i(\mathbf{z}'_i), \quad (2)$$

where the decoder f'_i and flow inverse function g'_i are inversions of the encoder f_i and flow function g respectively, and \mathbf{z}'_i can be \mathbf{z}_i or randomly sampled from $\mathcal{N}(\mathbf{0}, \mathbf{1})$. We illustrate hierarchical autoencoders and flows for rich and high-level spatial information with conditioning variables in either image space or latent space. In Fig. 1, we show a 4-level hierarchical normalising flow model, where each set of functions (f_i, g_i, g'_i, f'_i) corresponds to one level and where g'_i and f'_i are conditioned on the higher-level reconstruction, that is

$$\mathbf{x}'_1 = f'_1 \circ g'_1(\mathbf{z}'_1 | f'_2 \circ g'_2(\mathbf{z}'_2 | f'_3 \circ g'_3(\mathbf{z}'_3 | f'_4 \circ g'_4(\mathbf{z}'_4))))). \quad (3)$$

The model is learned in two phases: joint learning of all autoencoders $\{f_i, f'_i\}$ and then joint learning of all flows $\{g_i, g'_i\}$ with the pretrained autoencoders, for all $i \in \{1, 2, 3, 4\}$. The loss function for autoencoder learning, denoted \mathcal{L}_{ae} , is the mean squared error (MSE) between the reconstructed data and the processed data, and for the learning of flows the objective is to minimise the negative log-probability of \mathbf{y}_i , denoted $\mathcal{L}_{\text{flow}}$, such that the represented distribution of the latent variable is modelled to be the standard Gaussian distribution, from which a random latent variable can be sampled for data generation. Given N pixels and c channels ($c = 3$ for an RGB image and $c = 1$ for a greyscale image), \mathbf{x}_i at level i can be represented as $\mathbf{x}_i = \{\mathbf{x}_{ij}\}$ for all $j \in \{1, \dots, N\}$, the autoencoder loss is then given by

$$\mathcal{L}_{\text{ae}}(\mathbf{x}'_i, \mathbf{x}_i) = \frac{1}{cN} \sum_{j=1}^N \|\mathbf{x}'_{ij} - \mathbf{x}_{ij}\|^2, \quad (4)$$

and the flow loss for the latent at level i is the negative log-probability of \mathbf{y}_i , that is $\mathcal{L}_{\text{flow}}(\mathbf{y}_i) = -\log p_Y(\mathbf{y}_i)$, using the change of variables as

$$\log p_Y(\mathbf{y}_i) = \log p_Z(\mathbf{z}_i) + \log |\det \nabla_Y g_i(\mathbf{y}_i)| = \log p_Z(\mathbf{z}_i) + \log |J_Y(g_i(\mathbf{y}_i))| , \quad (5)$$

where

$$\log p_Z(\mathbf{z}_i) = -\frac{1}{d_i} \log \frac{1}{(\sqrt{2\pi})^{d_i}} \exp\left(-\frac{1}{2}\|\mathbf{z}_i\|^2\right) = \frac{1}{2} \log 2\pi + \frac{1}{2d_i} \|\mathbf{z}_i\|^2 , \quad (6)$$

d_i is the dimension of the i th latent and $J_X(\cdot)$ computes the Jacobian matrix over the partial derivative X . Similarly, the log-probability of \mathbf{x}_i at level i is

$$\begin{aligned} \log p_X(\mathbf{x}_i) &= \log p_Z(\mathbf{z}_i) + \log |\det \nabla_X (g_i \circ f_i(\mathbf{x}_i))| \\ &= \log p_Z(\mathbf{z}_i) + \log |\det J_Y(g_i(\mathbf{y}_i))| + \log |\det J_X(f_i(\mathbf{x}_i))| . \end{aligned} \quad (7)$$

Then, the log-probability of an image at level i with hierarchical autoencoders and flows from multiple downsampling layers, $\mathbf{x}_{i+1} = d(\mathbf{x}_i)$ at level i , can be calculated with the chain rule as

$$\log p(\mathbf{x}_i) = \sum_{j=1}^i \log p_X(\mathbf{x}_j) + \log |\det J_X(d(\mathbf{x}_{j-1}))| \cdot \mathbf{1}[j > 1] , \quad (8)$$

where $[\cdot]$ is a binary indicator.

2.2 Diffusion Models

Differently from normalising flow models that sample in a low-dimensional embedding space due to the otherwise large computational complexity, diffusion models diffuse every image pixel in the image space independently, enabling pixelwise sampling from the Gaussian distribution.

2.2.1 Non-Markovian Gaussian Sampling

The forward and backward processes of a denoising diffusion probabilistic model (DDPM) (Ho et al., 2020) are defined as

$$\text{forward process: } q(\mathbf{x}_t|\mathbf{x}_{t-1}) := \mathcal{N}(\mathbf{x}_t; \sqrt{\alpha_t}\mathbf{x}_{t-1}, (1 - \alpha_t)\mathbf{I}) , \quad (9)$$

$$\text{backward process: } p_\theta(\mathbf{x}_{t-1}|\mathbf{x}_t) := \mathcal{N}(\mathbf{x}_{t-1}; \boldsymbol{\mu}_\theta(\mathbf{x}_t, t), \boldsymbol{\Sigma}_\theta(\mathbf{x}_t, t)) , \quad (10)$$

where t is the discretised sampling time step and α_t is the diffusion weight. The forward process can also be represented with a one-step diffusion from the clean input \mathbf{x}_0 as

$$q(\mathbf{x}_t|\mathbf{x}_0) = \mathcal{N}(\mathbf{x}_t; \sqrt{\bar{\alpha}_t}\mathbf{x}_0, (1 - \bar{\alpha}_t)\mathbf{I}) , \quad (11)$$

where $\bar{\alpha}_t = \prod_{i=1}^t \alpha_i$ is the accumulated weight at time t . The process of obtaining \mathbf{x}_t is Markovian due to requiring only \mathbf{x}_{t-1} . However, the backward steps do not need to be Markovian to satisfy the Gaussian form, but can jump multiple steps Δt at each transition, as shown in Def. 2.1. While the distribution of $\mathbf{x}_{t-\Delta t}$ in the backward process is clearly not Gaussian (except when $(t - \Delta t)$ is sufficiently large, say at the final forward step T), this assumption is reasonable for small Δt and facilitates an efficient backward process for which the data probability can be obtained, in contrast to the denoising diffusion implicit model

(DDIM) (Song et al., 2021). Example images generated using this strategy are shown in Fig. 6 for all $\Delta t \in \{1, 2, 10, 100\}$.

DEFINITION 2.1. A non-Markovian Gaussian backward process can be defined as

$$\begin{aligned} p_\theta(\mathbf{x}_{t-\Delta t}|\mathbf{x}_t) &= \mathcal{N}(\mathbf{x}_{t-\Delta t}|\tilde{\boldsymbol{\mu}}_\theta(\mathbf{x}_t, t, \Delta t), \tilde{\boldsymbol{\epsilon}}(t, \Delta t)) \\ &= \mathcal{N}\left(\mathbf{x}_{t-\Delta t} \middle| \sqrt{\frac{\bar{\alpha}_{t-\Delta t}}{\bar{\alpha}_t}}\mathbf{x}_t - \frac{\bar{\alpha}_{t-\Delta t} - \bar{\alpha}_t}{\sqrt{\bar{\alpha}_t\bar{\alpha}_{t-\Delta t}}(1 - \bar{\alpha}_t)}\boldsymbol{\epsilon}_\theta^t(\mathbf{x}_t), \frac{(\bar{\alpha}_{t-\Delta t} - \bar{\alpha}_t)(1 - \bar{\alpha}_{t-\Delta t})}{\bar{\alpha}_{t-\Delta t}(1 - \bar{\alpha}_t)}\mathbf{I}\right), \end{aligned} \quad (12)$$

where $\boldsymbol{\epsilon}_\theta^t(\mathbf{x}_t)$ is the estimated denoising gradient from a DDPM from time t to time 0, towards \mathbf{x}_0 from \mathbf{x}_t . For small Δt , this is a good approximation to the diffusion backward process. We provide a justification for defining the backward process in this way in the appendix.

2.2.2 Maximum Likelihood Estimation

The probability of an image can be calculated by using the forward and backward processes for each step of a pretrained diffusion model. The joint probability $p(\mathbf{x}_{0:T})$ and probability of the clean input \mathbf{x}_0 can be calculated by using the forward and backward conditional probability, $q(\mathbf{x}_{t+\Delta t}|\mathbf{x}_t)$ and $p_\theta(\mathbf{x}_t|\mathbf{x}_{t+\Delta t})$ respectively, at each pair of sampling steps $(t, t + \Delta t)$ following the Markov chain rule as

$$p(\mathbf{x}_{0:T}) = q(\mathbf{x}_0) \prod_{t=0}^{T-1} q(\mathbf{x}_{t+\Delta t}|\mathbf{x}_t) = p(\mathbf{x}_T) \prod_{t=0}^{T-1} p_\theta(\mathbf{x}_t|\mathbf{x}_{t+\Delta t}), \quad (13)$$

$$q(\mathbf{x}_0) = \frac{p(\mathbf{x}_T) \prod_{t=0}^{T-1} p_\theta(\mathbf{x}_t|\mathbf{x}_{t+\Delta t})}{\prod_{t=0}^{T-1} q(\mathbf{x}_{t+\Delta t}|\mathbf{x}_t)}. \quad (14)$$

Then the negative log-probability of the input image \mathbf{x}_0 is

$$-\log q(\mathbf{x}_0) = -\log p(\mathbf{x}_T) + \sum_{t=0}^{T-1} \left(\underbrace{\log q(\mathbf{x}_{t+\Delta t}|\mathbf{x}_t)}_{\text{forward process}} - \underbrace{\log p_\theta(\mathbf{x}_t|\mathbf{x}_{t+\Delta t})}_{\text{backward process}} \right). \quad (15)$$

Given an N -dimensional data point \mathbf{x} and an element-wise Gaussian distribution $\mathcal{N}(\boldsymbol{\mu}_c, \sigma_c^2)$, we have

$$-\log p(\mathbf{x}) = \frac{1}{2} \left(N \log 2\pi + \sum_{c=1}^N \log \sigma_c^2 \right) + \frac{1}{2} \sum_{c=1}^N \frac{(\mathbf{x}_c - \boldsymbol{\mu}_c)^2}{\sigma_c^2}. \quad (16)$$

Computing Eq. (15) can be decomposed into three steps:

1) *Calculating $\log p(\mathbf{x}_T)$.* Since \mathbf{x}_0 is fully diffused after T forward steps, \mathbf{x}_T follows the standard Gaussian distribution $\mathcal{N}(\mathbf{0}, \mathbf{1})$, and thus the negative log-likelihood only depends on the Gaussian noise.

2) *Calculating $\log q(\mathbf{x}_{t+\Delta t}|\mathbf{x}_t)$.* Since $\mathbf{x}_{t+1} = \sqrt{\alpha_{t+1}}\mathbf{x}_t + \sqrt{1 - \alpha_{t+1}}\boldsymbol{\epsilon}_{t \rightarrow t+1}$, it is easy to derive that

$$\mathbf{x}_{t+\Delta t} = \sqrt{\frac{\bar{\alpha}_{t+\Delta t}}{\bar{\alpha}_t}}\mathbf{x}_t + \sqrt{1 - \frac{\bar{\alpha}_{t+\Delta t}}{\bar{\alpha}_t}}\boldsymbol{\epsilon}_{t+\Delta t}, \quad (17)$$

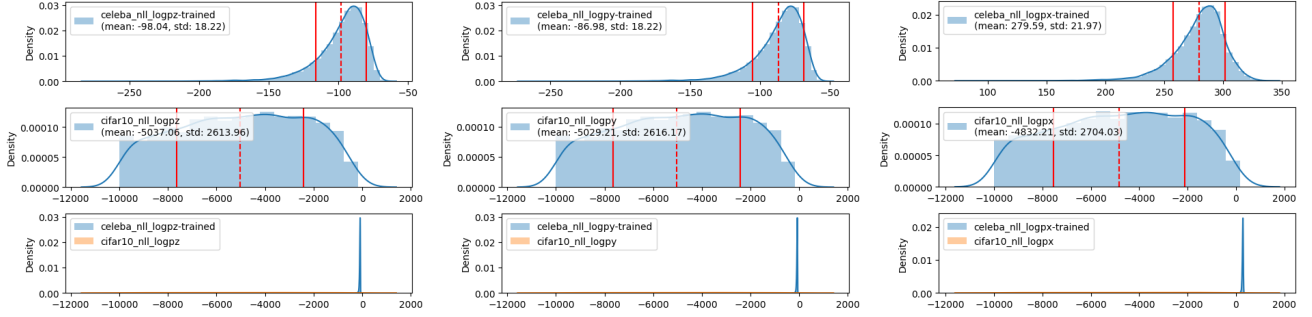

 Figure 2a. $\log p(\mathbf{z})$

 Figure 2b. $\log p(\mathbf{y})$

 Figure 2c. $\log p(\mathbf{x})$

Figure 2. Log-likelihood estimation using hierarchical autoencoders and flows. The encoder and flow are trained on CelebA and evaluated on CelebA and CIFAR10. The x-axis is $\log p(\cdot)$ and the y-axis is the histogram density. In each subfigure, the first row is on the in-distribution dataset CelebA and the second row is on out-of-distribution CIFAR10, both are in the last row. In (A), $\log p(\mathbf{z})$ can detect outlier samples, and adding $\log |\det(\cdot)|$ from NF and autoencoder does not significantly affect the distribution tendency, see (B) and (C). For better visualisation, samples with $\log p(\cdot)$ less than -10,000 are filtered out.

giving the mean and deviation of a Gaussian distribution as

$$\boldsymbol{\mu}(\mathbf{x}_t, t, \Delta t) = \sqrt{\frac{\bar{\alpha}_{t+\Delta t}}{\bar{\alpha}_t}} \mathbf{x}_t, \quad \sigma^2(t, \Delta t) = 1 - \frac{\bar{\alpha}_{t+\Delta t}}{\bar{\alpha}_t}. \quad (18)$$

3) *Calculating $\log p_\theta(\mathbf{x}_t | \mathbf{x}_{t+\Delta t})$.* In Def. 2.1, the estimation of \mathbf{x}_t follows a Gaussian distribution with

$$\boldsymbol{\mu}(\mathbf{x}_{t+\Delta t}, t, \Delta t) = \frac{(1 - \bar{\alpha}_t) \sqrt{\bar{\alpha}_{t+\Delta t}} \mathbf{x}_{t+\Delta t} + (\bar{\alpha}_t - \bar{\alpha}_{t+\Delta t}) \frac{\mathbf{x}_{t+\Delta t} - \sqrt{1 - \bar{\alpha}_{t+\Delta t}} \boldsymbol{\epsilon}_\theta^{t+\Delta t}(\mathbf{x}_{t+\Delta t})}{\sqrt{\bar{\alpha}_{t+\Delta t}}}}{\sqrt{\bar{\alpha}_t} (1 - \bar{\alpha}_{t+\Delta t})}, \quad (19)$$

$$\sigma^2(t, \Delta t) = \frac{(\bar{\alpha}_t - \bar{\alpha}_{t+\Delta t})(1 - \bar{\alpha}_t)}{\bar{\alpha}_t (1 - \bar{\alpha}_{t+\Delta t})}. \quad (20)$$

2.3 Experiments

Experiments on the hierarchical normalising flow models and the diffusion models, corresponding to Section 2.1 and Section 2.2 respectively, are provided below.

2.3.1 Experiments on Hierarchical Normalising Flow Models

Probability Density Estimation. Fig. 2 illustrates the probability density estimation on level 3 for an in-distribution dataset CelebA and an out-of-distribution dataset CIFAR10. The distribution of the latent variable \mathbf{z}_i of CelebA is concentrated on a lower mean value than that of CIFAR10 due to the learning of \mathbf{z}_i in the standard Gaussian distribution. Similarly, this distribution tendency is not changed in the image space illustrated by $\log p(\mathbf{x}_i)$. In this case, outlier samples from the in-distribution dataset can be detected with a small probability in the probability estimation.

Random Image Generation. Image reconstructions with encoded latent variables and conditional images as well as random samples are provided in Fig. 3. For the low-level autoencoder and flow, say at level 1, conditioned on the sequence of decoded \mathbf{x}_i for $i = \{2, 3, 4\}$, the reconstruction of \mathbf{x}_1 is close to the processed images although some human facial details are lost due to the downsampling mechanism, see



Figure 3a. Reconstruction with $\{z_i\}$ from encoders $\{g_i\}$ and conditional images from $\{f'_i\}$.

Figure 3b. Random generation with latent variables $\{z_i\} \sim \mathcal{N}(\mathbf{0}, \mathbf{1})$ and conditional images from $\{f'_i\}$.

Figure 3. Image generation on the end-to-end training of 4-level autoencoders and flows.

Fig. 3(A). While randomly sampling $\{z_i\}$ from the normal distribution at each level, the generated human faces are smooth but with blurry details in such as hair and chin and lack a realistic background.

Image Super-resolution. With the jointly trained autoencoders and flows on CelebA, the images with low resolution, $3 \times 8 \times 8$ (channel \times height \times width) and $3 \times 16 \times 16$, are decoded to $3 \times 64 \times 64$ with smooth human faces, see Fig. 4(A) and Fig. 4(B) respectively. The low-resolution image x_i is used as a condition image for 1) NF inverse $\{g'_i\}$ to generate embedding code to combine with the randomly sampled $z_i \sim \mathcal{N}(\mathbf{0}, \mathbf{1})$ and 2) decoders $\{f'_i\}$ to concatenate with all upsampling layers in each decoder. This preserves the human facial details from either high levels or low levels for realistic image generation. As the resolution of the low-resolution images increases, the embedding code contains richer details.



Figure 4a. Resolution: $3 \times 8 \times 8$ to $3 \times 64 \times 64$

Figure 4b. Resolution: $3 \times 16 \times 16$ to $3 \times 64 \times 64$

Figure 4. Image super-resolution on dataset CelebA. The first column are low-resolution images, the second column are real images, and the rest are high-resolution images with latent variables $\{Z_i\} \sim \mathcal{N}(\mathbf{0}, \mathbf{1})$ conditioned on the low-resolution images and temperature 1.0.

2.3.2 Experiments on Diffusion Models

Log-likelihood Estimation on Point Samples. We evaluate the log-probability of each point of point samples including Swiss roll, circle, moon, and S shown in Fig. 5. Given a pretrained diffusion model on Swiss roll samples with 100 forward steps with each diffused by random Gaussian noise (see Fig. 5(A), the log-probability of the samples in Fig. 5(B) follows Eq. (15) with $\Delta t = 1$ and indicates higher probability and density on seen or similar samples than unseen ones. In Figs. 5(B)-(C), the mean value of the Swiss roll sample achieves a higher mean value, -0.933, and a higher histogram density, 0.7, than the others. As

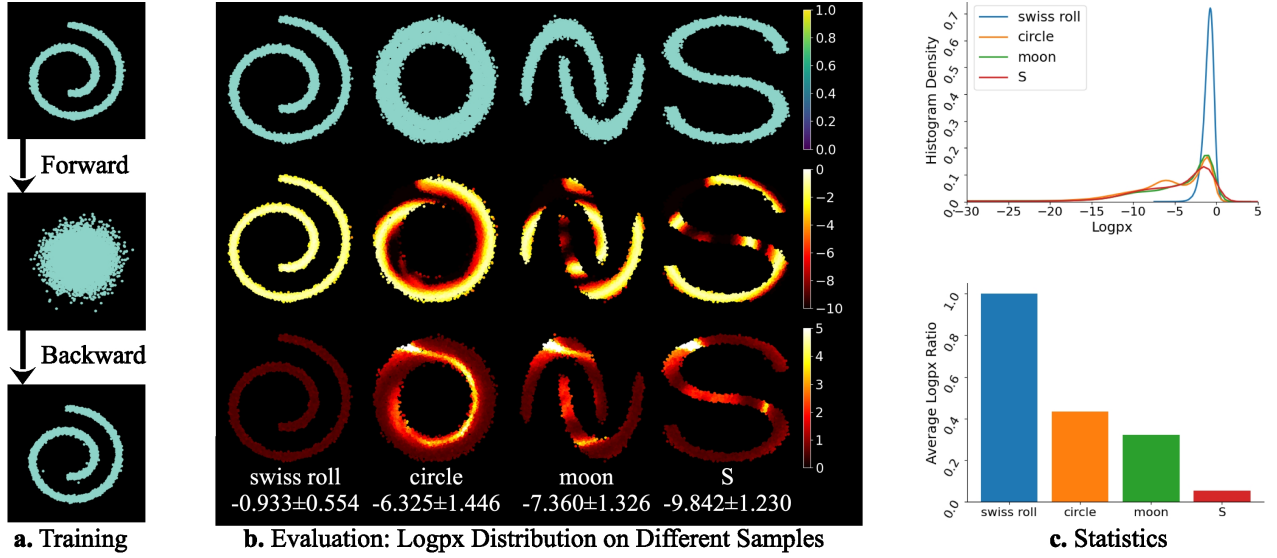


Figure 5. Evaluation of log-probability of x_0 on point samples with each of 10,000 points. (A) The training is on a Swiss roll sample and a diffusion model with forward (noising) and backward (denoising) processes. (B) At the evaluation phase, unseen samples, that is circle, moon, and S, have lower $\log p(x)$ values than the seen Swiss roll sample. In b, the first row is sampled points and the middle and last rows are the mean value and the standard deviation of $\log p(x)$ for each point on 100 random rounds respectively, which is represented as “mean \pm std”. The randomness lies in the random noise in the forward and backward processes. Lighter colour indicates higher density. (C) Statistics indicates the higher density of a seen sample (Swiss roll) than an unseen one (circle, moon, or S) through the diffusion model by using the negative of Eq. (15) with \log_{10} .



Figure 6a. $\Delta t = 1$

Figure 6b. $\Delta t = 2$

Figure 6c. $\Delta t = 10$

Figure 6d. $\Delta t = 100$

Figure 6. Image generation from our modified DDPM with step size Δt . Samples follow a Gaussian distribution, as shown in Def. 2.1. Fine details are obtained even for very large steps ($\Delta t = 100$).

the difference in the sample shape from the Swiss roll increases, the log-likelihood decreases, as shown in the bar chart in Fig. 5(C). It indicates that sampling from a low-density distribution is unable to reverse the diffusion step to obtain a realistic sample from the training set.

DDPM Sampling with Large Steps. While Fig. 5 uses $\Delta t = 1$ as the standard DDPM sampling process, it is feasible to sample with a fairly large step without losing the sample quality. This enables sampling from the Gaussian distribution for the log-likelihood estimation with less running time. To visualise the image quality, we evaluate the samples on CelebA dataset by using a pretrained diffusion model with 1,000 forward diffusion steps. In Fig. 6, the sampling uses Def. 2.1 with an increase step in $\{2, 10, 100\}$ while the samples have a high quality for $\Delta t = \{2, 10\}$ and a fair quality for $\Delta t = 100$.

Higher-order Solution Stabilises Sampling. While sampling with a large step Δt can sometimes cause bias from the one with a small Δt , the higher-order method, mainly the Runge–Kutta method (RK4) (Runge, 1895; Kutta, 1901) in our case, effectively alleviates such a bias. See the appendix for our implementation of RK4. We evaluate both the point samples and human face images from CelebA. In Fig. 7, compared with the sample by using DDPM, RK4 with DDPM inference achieves less noise at $\Delta t = \{2, 5, 10\}$. For $\Delta t = 20$, RK4 performs expectedly worse because it only applies 5 sampling steps while the training is on ($T = 100$) diffusion steps. In Fig. 8, we apply DDIM as the inference method for RK4 to deterministically compare the samples with DDIM. As Δt increases from 1 to 100, many of the samples using DDIM lose the image consistency with the samples at $\Delta t = 1$; however, most of the samples using RK4 still retain the image consistency. This indicates the robustness of applying RK4 with a large sampling step.



Figure 7. Sampling robustness of DDPM and RK4 @ step Δt . With Δt being 5 or 10, RK4 still achieves clear sampling compared with DDPM. If Δt is too large, for instance 20, RK4 fails as expected.



Figure 8a. DDIM@1

Figure 8b. DDIM@2

Figure 8c. DDIM@10

Figure 8d. DDIM@100



Figure 8e. RK4@1

Figure 8f. RK4@2

Figure 8g. RK4@10

Figure 8h. RK4@100

Figure 8. Random image generation using DDIM and RK4 with DDIM as inference @ time step $\Delta t = \{1, 2, 10, 100\}$. The RK4 sampling method is more robust than DDIM, especially at $\Delta t = 100$, with a higher image consistency than those at $\Delta t = 1$.

3 ADVERSARIAL ATTACKS AND DEFENCES

3.1 Bounded Patch Attack

In contrast to full image-level attacks like ℓ_2 and ℓ_∞ bounded attacks, patch attacks, which are ℓ_0 bounded attacks, aim to restrict the number of perturbed pixels. These attacks are more feasible to implement in real-world settings, resulting in border impacts. Below, we conduct an initial investigation into the defence against patch attacks by leveraging the knowledge of the data manifold.

3.1.1 Formulation

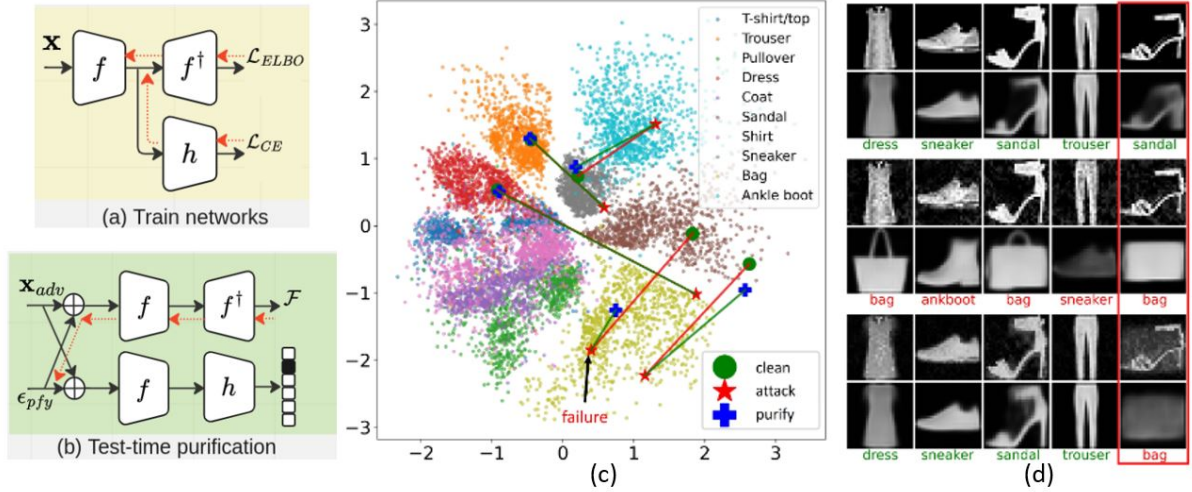


Figure 9. The framework of adversarial purification for imagewise adversarial attacks. (A) Jointly train the classifier with the ELBO loss. (B) Test time adversarial purification with the ELBO loss. (C) Trajectories of clean (green) - attack (red) - purified (blue) images on a 2D latent space. (D) Input images and reconstruction images of samples in (C). The top two rows are the input and reconstruction of clean images, the middle two rows are the input and reconstruction of adversarial images. The bottom two rows are the input and reconstruction of purified images. The text represents predicted classes with green colour for correct predictions and red colour for incorrect predictions. The red box on the right corresponds to the failure case (purified process fails).

We briefly describe the adversarial purification framework in Yang et al. (2022) and focus more on extending the framework to defend the ℓ_0 bounded attacks. We define the real-world high-dimensional data as $\mathbf{x} \in \mathbb{R}^n$ which lies on a low-dimensional manifold \mathcal{M} diffeomorphic to \mathbb{R}^m with $m \ll n$. We define an encoder function $\mathbf{f} : \mathbb{R}^n \rightarrow \mathbb{R}^m$ and a decoder function $\mathbf{f}^\dagger : \mathbb{R}^m \rightarrow \mathbb{R}^n$ to form an autoencoder. For a point $\mathbf{x} \in \mathcal{M}$, \mathbf{f}^\dagger and \mathbf{f} are approximate inverses. We define a discrete label set \mathcal{L} of c elements as $\mathcal{L} = \{1, \dots, c\}$ and a classifier in the latent space as $\mathbf{h} : \mathbb{R}^m \rightarrow \mathcal{L}$. The encoder maps the image \mathbf{x} to a lower-dimensional vector $\mathbf{z} = \mathbf{f}(\mathbf{x}) \in \mathbb{R}^m$ and the functions \mathbf{f} and \mathbf{h} together form a classifier in the image space $\mathbf{h}(\mathbf{z}) = (\mathbf{h} \circ \mathbf{f})(\mathbf{x}) \in \mathcal{L}$.

We define three sets of parameters: 1) ϕ parametrises the encoder distribution, denoted as $q_\phi(\mathbf{z}|\mathbf{x})$, 2) θ parametrises the decoder distributions, represented as $p_\theta(\mathbf{x}|\mathbf{z})$, and 3) ψ parametrises the classification head, given by $\mathbf{h}_\psi(\mathbf{z})$. These parameters are jointly optimised with respect to the ELBO loss and the cross-entropy loss as shown in Eq. (21), where λ is the trade-off term between the ELBO and the classification loss. By adopting this formulation, we notice a remarkable semantic consistency between the decoder and the classifier. Specifically, when making predictions on adversarial examples, if the predicted label is “bag”, we observe that the reconstructed image tends to resemble a “bag” as well. This phenomenon is illustrated in Fig. 9(D) and Fig. 10.

$$\max_{\theta, \phi, \psi} \underbrace{\mathbb{E}_{\mathbf{z} \sim q_{\phi}(\mathbf{z}|\mathbf{x})} [\log p_{\theta}(\mathbf{x}|\mathbf{z})] - D_{KL}[q_{\phi}(\mathbf{z}|\mathbf{x}) \| p(\mathbf{z})]}_{\text{ELBO (lower bound of } \log p_{\theta}(\mathbf{x}))} + \underbrace{\lambda \mathbb{E}_{\mathbf{z} \sim q_{\phi}(\mathbf{z}|\mathbf{x})} [\mathbf{y}^T \log \mathbf{h}_{\psi}(\mathbf{z})]}_{\text{Classification loss}}. \quad (21)$$

To defend the imagewise attack, a purification vector can be obtained through the test-time optimisation over the ELBO loss. For example, given an adversarial example \mathbf{x}_{adv} , a purified sample can be obtained by $\mathbf{x}_{\text{pfy}} = \mathbf{x}_{\text{adv}} + \boldsymbol{\epsilon}_{\text{pfy}}$ with

$$\boldsymbol{\epsilon}_{\text{pfy}} = \arg \max_{\boldsymbol{\epsilon} \in \mathcal{C}_{\text{pfy}}} \mathbb{E}_{\mathbf{z} \sim q_{\phi}(\mathbf{z}|\mathbf{x}_{\text{adv}} + \boldsymbol{\epsilon})} [\log p_{\theta}(\mathbf{x}_{\text{adv}} + \boldsymbol{\epsilon}|\mathbf{z})] - D_{KL}[q_{\phi}(\mathbf{z}|\mathbf{x}_{\text{adv}} + \boldsymbol{\epsilon}) \| p(\mathbf{z})], \quad (22)$$

where $\mathcal{C}_{\text{pfy}} = \{\boldsymbol{\epsilon} \in \mathbb{R}^n \mid \mathbf{x}_{\text{adv}} + \boldsymbol{\epsilon} \in [0, 1]^n \text{ and } \|\boldsymbol{\epsilon}\|_p \leq \epsilon_{\text{th}}\}$ which is the feasible set for purification and ϵ_{th} is the purification budget.

When compared to ℓ_{∞} attacks, ℓ_0 attacks, such as the adversarial patch attacks, introduce larger perturbations to the perturbed pixels. Therefore, we decide to remove the feasible set constraints \mathcal{C}_{pfy} for the patch-attack purification. Without these constraints, the purified examples can take on any values within the image space. In our experiments, however, we observed intriguing phenomena, see the results below.

3.2 Experiments

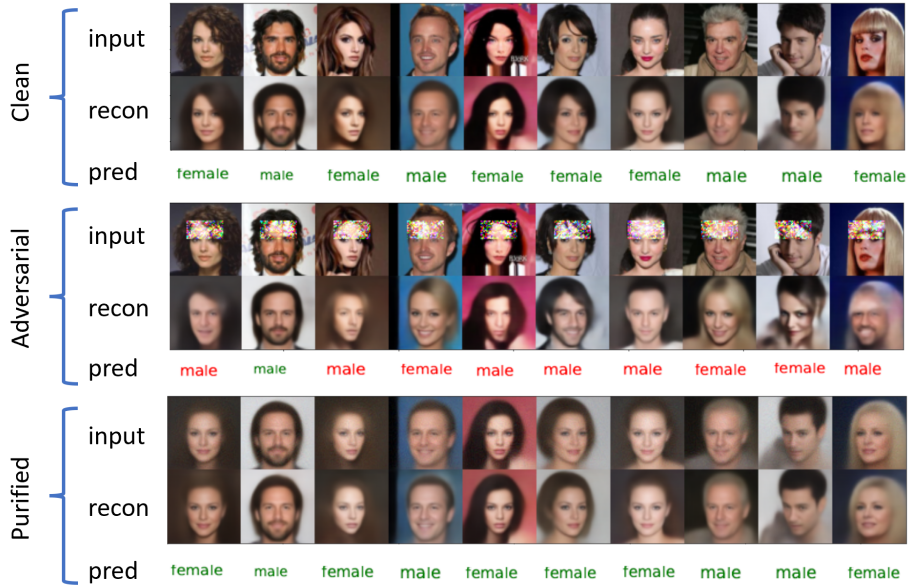


Figure 10. Class predictions from the VAE-Classifier models on clean, adversarial and purified samples of the CelebA gender attribute. The top two rows are the input and reconstruction of clean images, the middle two rows are the input and reconstruction of patch adversarial images. The bottom two rows are the input and reconstruction of purified images. The text represents the predicted classes with **green** colour for correct predictions and **red** colour for incorrect predictions. Since predictions and reconstructions from the VAE classifier are correlated, our test-time defences are effective against adversarial attacks.

Table 1. Classification accuracy of the model on clean and adversarial (patch) examples.

Dataset + Backbone	VAE-CLF			+TTD (ELBO)		
	Clean	Patch-PGD	Patch-NAG	Clean	Patch-PGD	Patch-NAG
CelebA-Gender (ResNet-50)	97.86	13.14	6.83	91.20	75.75	76.75

We use the gender classification model (Yang et al., 2022) to demonstrate the adversarial purification of ℓ_0 bounded attacks. To ensure that the adversarial examples do not alter the semantic content of the images, we restrict the perturbation region to the forehead of a human face. The patch for perturbation is a rectangular shape measuring 16×32 , see Fig. 10. For the patch attacks, we conduct 2,048 iterations with step size $1/255$ using PGD (Madry et al., 2018) and PGD-NAG (Nesterov Accelerated Gradient) (Lin et al., 2020). In Table 1, the purification is carried out through 256 iterations with the same step size.

4 SEMANTIC DISENTANGLEMENT ON MANIFOLD

4.1 GridVAE for Clustering and Disentanglement

4.1.1 Formulation

A variational autoencoder (VAE) (Kingma and Welling, 2013) is a neural network that maps inputs to a distribution instead of a fixed vector. Given an input x , the encoder with neural network parameters ϕ maps it to a hidden representation z . The decoder with the latent representation z as its input and the neural network parameters as θ reconstructs the output to be as similar to the input x . We denote the encoder $q_\phi(z|x)$ and decoder $p_\theta(x|z)$. The hidden representation follows a prior distribution $p(z)$.

With the goal of making the posterior $q_\phi(z|x)$ close to the actual distribution $p_\theta(z|x)$, we minimise the Kullback-Leibler divergence between these two distributions. Specifically, we aim to maximise the log-likelihood of generating real data while minimising the difference between the real and estimated posterior distribution by using the evidence lower bound (ELBO) as the VAE loss function

$$L(\theta, \phi) = -\log p_\theta(x) + D_{KL}(q_\phi(z|x)||p_\theta(z|x)) = -\mathbb{E}_{z \sim q_\phi(z|x)} \log p_\theta(x|z) + D_{KL}(q_\phi(z|x)||p_\theta(z)) , \quad (23)$$

where the first term is the reconstruction loss and the second term is the regularisation for $q_\phi(z|x)$ to be close to $p_\theta(z)$. The prior distribution of z is often chosen to be a standard unit isotropic Gaussian, which implies that the components of z should be uncorrelated and hence disentangled. If each variable in the latent space is only representative of a single element, we assume that this representation is disentangled and can be well interpreted.

Emergent language (EL) (Havrylov and Titov, 2017) is hereby introduced as a language that arises spontaneously in a multi-agent system without any pre-defined vocabulary or grammar. EL has been studied in the context of artificial intelligence and cognitive science to understand how language can emerge from interactions between agents. EL has the potential to be compositional such that it allows for referring to novel composite concepts by combining individual representations for their components according to systematic rules. However, for EL to be compositional, the latent space needs to be disentangled (Chaabouni et al., 2020). Hence, we integrate VAE into the EL framework by replacing the sender LSTM with the encoder of the VAE noting that the default LSTM encoder will entangle the symbols due to its sequential structure where the previous output is given as the input to the next symbol. In contrast, the symbols can be disentangled with a VAE encoder.

To achieve disentangled representations in EL, the VAE encoder must be able to cluster similar concepts into discrete symbols that are capable of representing attributes or concepts. The standard VAEs are powerful, but their prior distribution, which is typically the standard Gaussian, is inferior in clustering tasks, particularly the location and the number of cluster centres. In the EL setting, we desire a posterior

distribution with multiple clusters, which naturally leads to an MoG prior distribution with K components

$$p(z) = \frac{1}{K} \sum_{k=1}^K \mathcal{N}(z | \mu_k, \sigma_k^2). \quad (24)$$

We choose the μ_k to be located on a grid in a Cartesian coordinate system so that the posterior distribution clusters can be easily determined based on the sample's distance to a cluster centre. We refer to this new formulation as GridVAE, which is a VAE with a predefined MoG prior on a grid. The KL-divergence term in Eq. (23) can be re-written as

$$D_{KL}(q_\phi(z|x) || p_\theta(z)) = \mathbb{E}_{x \sim p(x)} \mathbb{E}_{q_\phi(z|x)} [\log p(z) - \log q_\phi(z|x)]. \quad (25)$$

The log probability of the prior can be easily calculated with the MoG distribution, and we only need to estimate the log probability of the posterior using a large batch size during training. By using a GridVAE, we can obtain a posterior distribution with multiple clusters that correspond to the same discrete attribute, while allowing for variations within the same cluster to generate different variations of the attribute.

4.1.2 Experiments

We evaluate the clustering and disentanglement capabilities of the proposed GridVAE model using a two-digit MNIST dataset (LeCun et al., 1998) consisting of digits 0 to 5. Each digit is from the original MNIST dataset, resulting in a total of 36 classes [00, 01, 02, ..., 55].

To extract features for the encoder, we use a 4-layer ResNet (He et al., 2016) and its mirror as the decoder. The VAE latent space is 2-dimensional (2D), and if the VAE learns a disentangled representation, each dimension of the 2D latent space should represent one of the digits. We use a 2D mixture of Gaussian (MoG) as the prior distribution, with 6 components in each dimension centred at integer grid points from [-2, -1, 0, 1, 2, 3], that is the coordinates for the cluster centres are [(-2, -2), (-2, -1), ..., (3, 3)]. The standard deviation of the mixture of Gaussian is 1/3.

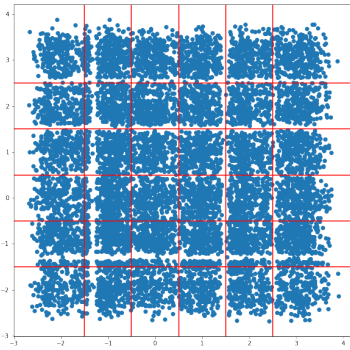


Figure 11. Scatter plot of test set latent space with an MoG prior.

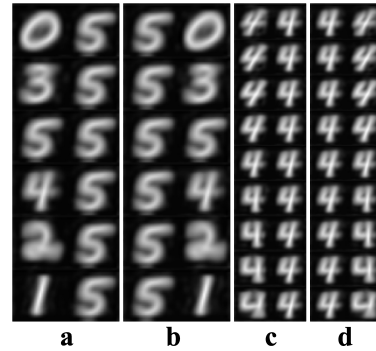


Figure 12. Generated images from sampling the latent space. (A) The second dimension is fixed at 0, changing the first dimension from -2 to +3. (B) The first dimension is fixed at 0 and the second dimension is changed from -2 to +3. (C) Around the cluster centre(1, 1), keep the second dimension fixed and change the first dimension. (D) Around the cluster centre(1, 1), keep the second dimension fixed and change the first dimension.

After training the model, we generate a scatter plot of the test set latent space, as shown in Fig. 11. Since the prior is a mixture of Gaussian on the grid points, if the posterior matches the prior, we can simply draw a boundary in the middle of two grid points, illustrated by the red lines in Fig. 11.

With the trained model, one can sample in the latent space for image generation. In Figs. 12 (A)-(B), when we decode from the cluster centres (i, j) : in (A) we keep $j = 0$ and change i from -2 to 3 , while in (B) we keep $i = 0$ and change j from -2 to 3 . The latent space is disentangled with respect to the two digits - the first dimension of the latent space controls the first digit, while the second dimension controls the second digit. Each of the cluster centres corresponds to a different number.

Figs. 12(C)-(D) show images generated within the cluster centred at $(1, 1)$, that is the pairs of number “44”. If we slightly modify one of the dimensions, it corresponds to different variations of the number “4” along this dimension, while keeping the other digit unchanged.

Overall, these results demonstrate the effectiveness of the proposed GridVAE model in clustering and disentangling the latent space on the two-digit MNIST dataset.

4.2 Scaling Up GridVAE

In Sec. 4.1, the two-digit MNIST dataset lies in a 2-dimensional latent space. However, many real-world datasets would require a much higher dimensional space.

4.2.1 Addressing Higher Dimensional Latent Space

Discretising a continuous space, such as in GridVAE, is challenging due to the curse of dimensionality (Bellman, 1957). This refers to the exponential growth in the number of clusters as the number of dimensions increases, which leads to a computational challenge when dealing with high-dimensional latent space. For example, when applying GridVAE to reconstruct images of the CelebA (Liu et al., 2015) dataset to learn the 40 attributes, we need a 40-dimensional latent space with two clusters in each dimension to represent the presence or absence of a given attribute. Firstly, parametrising the mixture of Gaussian prior $p(z) = \sum_{k=1}^K \mathcal{N}(z|\mu_k, \sigma_k^2)/K$ over 40 dimensions is prohibitively expensive as $K = 2^{40} \approx 1.1 \times 10^{12}$. Secondly, the assumption of equal probability for the components, which was appropriate for the simple 2-digit MNIST dataset, is no longer valid. This is because the attributes in the CelebA dataset are not uniformly distributed, and some combinations may not exist. For instance, the combination of “black hair” + “blonde hair” + “brown hair” + “bald” is impossible due to attribute conflicts. To address this issue, we use the proposed loss function in Eq. (23) incorporating relaxation.

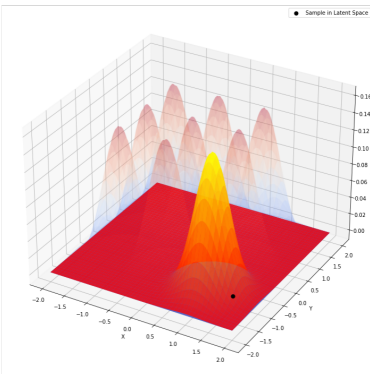


Figure 13. When calculating the KL-divergence, only the mixture component closest to the data (darker shade) is considered. Other components (lighter shade) are ignored. This can be generalised to multiple dimensions and multiple components in each dimension.

To avoid pre-parametrising $p(z)$ over 40 dimensions, we have implemented a dynamic calculation of the KL-divergence between q_ϕ and p_θ , whereby only the cluster that is closest to the latent space representation is considered, as illustrated in Fig. 13. This means that clusters to which the data point does not belong do not affect its distribution, and the MoG distribution is simplified to a multivariate Gaussian as

$$D_{\text{KL}}(p_1 \parallel p_2) = \frac{1}{2} \left[\log \frac{|\Sigma_2|}{|\Sigma_1|} - n + \text{tr}(\Sigma_2^{-1}\Sigma_1) + (\mu_2 - \mu_1)^T \Sigma_2^{-1}(\mu_2 - \mu_1) \right], \quad (26)$$

where $p_1 = q_\phi(z|x) = \mathcal{N}(z|\mu(x), \Sigma(x))$, $\Sigma = \text{diag}(\sigma_1^2, \dots, \sigma_n^2)$, $p_2 = \mathcal{N}(\mu_2, \Sigma_2)$, $\mu_2 = \text{R}(\mu_1)$, and $\Sigma_2 = \text{diag}(\sigma_0^2, \dots, \sigma_n^0)$ with the round function $\text{R}(\cdot)$ for the closest integer.

The key step here is that the round function dynamically selects the cluster centre closest to μ_1 , and σ_0 is a pre-defined variance for the prior distribution. It should be chosen so that two clusters next to each other have a reasonable degree of overlap, for example, $\sigma_0 = 1/16$ in some of our following experiments. The KL-divergence term becomes

$$\begin{aligned} D_{\text{KL}}(q_\phi(z|x) \parallel p_\theta(z)) &= \frac{1}{2} \left[\log \frac{|\Sigma_2|}{|\Sigma_1|} - n + \text{tr}(\Sigma_2^{-1}\Sigma_1) + (\mu_2 - \mu_1)^T \Sigma_2^{-1}(\mu_2 - \mu_1) \right] \\ &= \frac{1}{2} \left[\log \prod_i \sigma_0^2 - \log \prod_i \sigma_i^2 - n + \sum_i \frac{\sigma_i^2}{\sigma_0^2} + \sum_i \frac{(\mu_i - \text{R}(\mu_i))^2}{\sigma_0^2} \right] \\ &= \frac{1}{2} \left[\sum_{i=1}^n (\log \sigma_0^2 - \log \sigma_i^2 - 1) + \sum_{i=1}^n \frac{\sigma_i^2 + (\mu_i - \text{R}(\mu_i))^2}{\sigma_0^2} \right]. \end{aligned} \quad (27)$$

By adopting Eq. (27), we can significantly reduce the computational complexity of the model, even for a high-dimensional latent space, bringing it to a level comparable to that of a standard VAE. It is worth noting that the global disentanglement may no longer be guaranteed. Rather, the model only provides local disentanglement within the proximity of each cluster.

Upon training the GridVAE with a 40-dimensional latent space by using the proposed Eq. (27) on the CelebA dataset, we observe some intriguing disentanglement phenomena. Fig. 14 showcases the disentanglement of two latent space dimensions, where the first dimension governs one attribute and the second dimension determines another one. Combining these two dimensions leads to simultaneous attribute changes in the generated images.

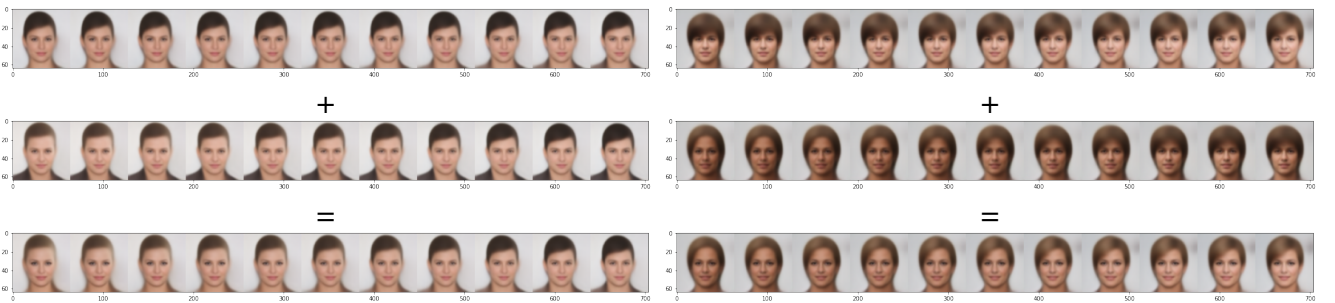


Figure 14. Two generated examples using linear sampling in the latent space. The top row fixes the dimensions and changes the first one from -0.5 to +1.5. The middle row fixes the dimensions and changes the second one from -0.5 to +1.5. The bottom row changes the first and second dimensions from -0.5 to +1.5.

An inherent limitation of this unsupervised approach is that while the latent space appears to be locally disentangled for each image, the same dimension may have different semantic interpretations across different images. To address this issue, we introduce all 40 attributes of the dataset during the training. This should establish an upper bound on the disentanglement.

4.2.2 From Unsupervised to Guided and Partially Guided GridVAE

To this end, we described an unsupervised approach to learning the latent space representation of images. However, for datasets like CelebA with ground truth attributes, we can incorporate them into the latent space to guide the learning. Specifically, we extract the 40-dimensional attribute vector indicating the presence or absence of each feature for each image in a batch and treat it as the ground truth cluster centre μ_i^{gt} . Hence, instead of rounding the latent space representation μ_i in Eq. (27), we replace it with μ_i^{gt} .

One limitation of this approach is the requirement of the ground truth attributes for all images, which may not always be available or feasible. Additionally, it is important to note that while we refer to this approach as “guided”, the given attribute information only serves in the latent space as the cluster assignment prior, and the VAE reconstruction task remains unsupervised. This differs from classical supervised learning, where the label information is the output. Furthermore, in our approach, no specific coordinate in the latent space is designated for the input. Instead, we provide guidance that the sample belongs to a cluster centred at a certain point in the latent space.

This guided learning framework can be extended to a subset of the 40 attributes or a latent space with more dimensions. For clarity, we will refer to the latter as “partially guided” to distinguish it from the commonly used “semi-supervised” by using a subset of the labelled dataset.

We conduct the experiments using attribute information as latent space priors and obtain the following findings for the guided approach: (a) GridVAE is able to cluster images accurately based on their attributes and the same dimension has the same semantic meaning across different images. For instance, dimension 31 represents “smile”. (b) GridVAE could not generate images for clusters that have little or no representation in the training set. For example, the attempt of generating an image of a bald female by constraining GridVAE to the “female” and “bald” clusters is not achievable for an accurate representation. (c) Some attributes are more universal across different images, such as their ability to add a smile to almost any face. However, other attributes, such as gender, are not always modifiable. This could be caused by attributes that are not independent and can be influenced by others. Universal attributes, such as “smile”, seem to primarily locate locally in the image region without interruption from the other attributes, see Fig. 15.

To further illustrate the incompleteness and correlation among the attributes in the CelebA dataset, we use a subset of the given attributes. We choose 38 out of the 40 attributes, excluding attributes 20 (female/male) and 31 (not smiling/smiling). Fig. 16 shows that the GridVAE cannot learn the omitted attributes. This highlights the interdependence of different attributes in the latent space.

4.3 Combining Manifolds of GridVAE Disentangled Attribute and Facial Recognition

After achieving a disentangled latent space, one may still wonder about the usefulness of a semantic description of a manifold. One can consider the scenario where another manifold, such as a facial recognition manifold, is learned. By studying these two manifolds jointly, we can gain insights to make the models more explainable and useful. One potential application is to better understand the relationship between facial attributes and facial recognition. By analyzing the disentangled latent space of facial attributes and the manifold learned for facial recognition, we can potentially identify which attributes are



Figure 15. Generated images from sampling in the latent space. Keeping all other dimensions fixed and changing dimension (A) 31 (smile) from -0.5 to +1.5, or (B) 20 (male) from -0.5 to +1.5.

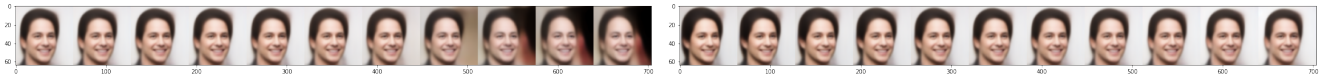


Figure 16. Partially guided GridVAE generation from the latent attributes which are not provided during training. The left and right rows are with the dimensions 20 and 31 respectively.

the most important for recognising different faces. This understanding can then be used to improve the performance of facial recognition models as well as explain the model decisions.

For instance, FaceNet (Schroff et al., 2015) directly learns a mapping from face images to a compact Euclidean space where distances correspond to a measure of face similarity. To discover the semantic structure of this manifold with x as binary attributes, we can follow these steps:

1. Build a face recognition manifold using contrastive learning.
2. Use the CelebA dataset with ground truth attribute labels (40 binary values).
3. Insert CelebA samples onto the recognition manifold.
4. Find the nearest neighbour for each CelebA sample using the face recognition manifold coordinates.
5. For each attribute in x , compute $p(x)$ over the entire CelebA dataset.
6. For each attribute in x , compute $p(x|x \text{ of nearest neighbour} = 0)$.
7. For each attribute in x , compute the KL divergence between $p(x)$ and $p(x|x \text{ of nearest neighbour} = 0)$.
8. Identify attributes with the largest KL divergence.

Fig. 17 demonstrates that the KL Divergence between $p(x)$ and $p(x|x \text{ of nearest neighbour} = 0)$ is significantly larger for certain attributes, such as “male”, “wearing lipstick”, “young” and “no beard”, than the others. This indicates that the neighbourhood structure of the facial recognition manifold is markedly different from the distribution of these attributes in the entire dataset. These findings highlight the importance of the joint study of different manifolds to gain a more profound understanding of the

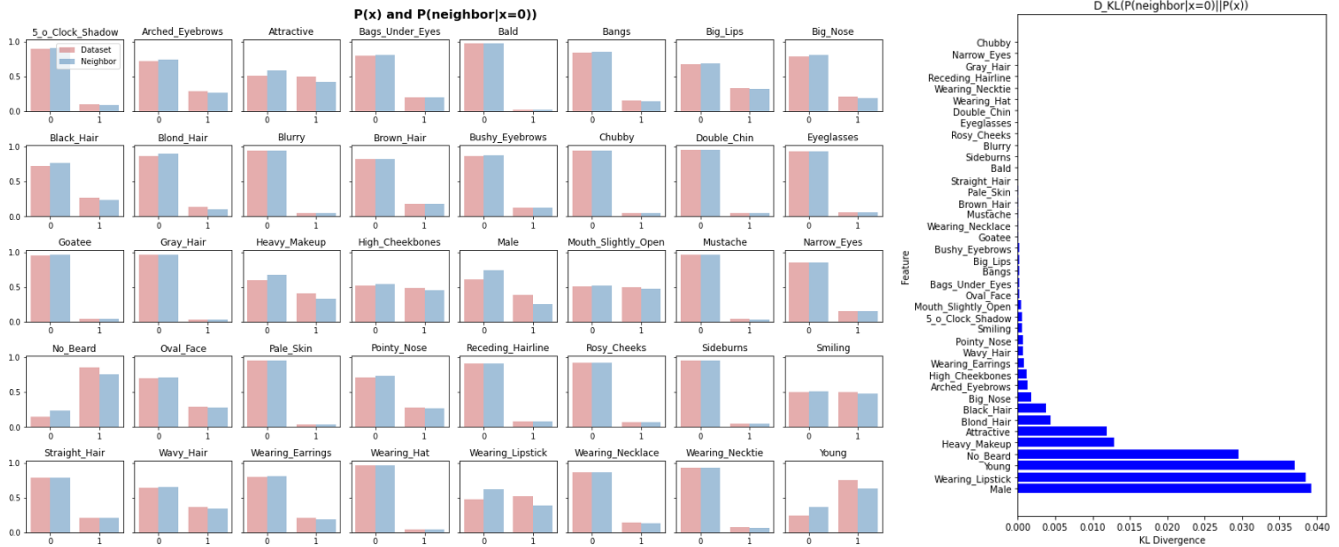


Figure 17a. $p(x)$ and $p(x|x \text{ of nearest neighbour} = 0)$ distributions. **Figure 17b.** KL divergence.

Figure 17. Semantic structure of the face recognition manifold by jointly studying the attribute manifold and the facial recognition manifold.

relationship between the attributes and the recognition tasks. By incorporating it into the models, we can potentially improve the performance of facial recognition models and also enhance their interpretability.

5 CONCLUSION

This work studies the image geometric representation from high-dimensional spatial space to low-dimensional latent space on image manifolds. To explore the image probability distribution with the assumption that real images are usually in a high-density region while not all samples from the distribution can be represented as realistic images, we incorporate log-likelihood estimation into the procedures of normalising flow and diffusion models. Patch attacks and defences are then applied in the image space to test the semantic consistency to evaluate the reconstruction robustness. We also consider an EL framework with the proposed GridVAE model to disentangle the elements of the latent variable on an image manifold for controllable and interpretable presentations with orthogonal semantics. Experiments show the effectiveness of probability estimation in distinguishing seen examples from unseen ones, the quality and the efficiency with large sampling steps in image generation, the well-preserved semantic consistency with patch attacks, and meaningful representations of varying specific element(s) of the latent variable to control object attribute(s) in the image space.

CONFLICT OF INTEREST STATEMENT

The authors declare that the research was conducted in the absence of any commercial or financial relationships that could be construed as a potential conflict of interest.

AUTHOR CONTRIBUTIONS

P. Tu and R. Hartley are the principal investigators of this project. Z. Xu, R. Hartley, J. Zhang and D. Campbell contributed to the maximum likelihood estimation section. Z. Yang and P. Tu contribute to the

attacks and defences section, and Y. Fu contributes to the semantic disentanglement section. All authors contribute to discussions and proofreading in this work.

FUNDING

This work is supported by the DARPA geometries of learning (GoL) project under the grant agreement number HR00112290075.

ACKNOWLEDGMENTS

We thank Amir Rahimi for his contribution to the code and discussion of the normalising flow models.

SUPPLEMENTAL DATA

Please refer to the appendix.

DATA AVAILABILITY STATEMENT

Datasets used in this work are available online, and our code with demonstrated samples will be released upon publication. For further inquiries, please contact the corresponding author.

APPENDIX

1 JUSTIFICATION FOR DEFINITION 2.1

DEFINITION 2.1. A non-Markovian Gaussian backward process can be defined as

$$p_\theta(\mathbf{x}_{t-\Delta t}|\mathbf{x}_t) = \mathcal{N}(\mathbf{x}_{t-\Delta t}|\tilde{\boldsymbol{\mu}}_\theta(\mathbf{x}_t, t, \Delta t), \tilde{\boldsymbol{\epsilon}}(t, \Delta t))$$

$$= \mathcal{N}\left(\mathbf{x}_{t-\Delta t}\left|\sqrt{\frac{\bar{\alpha}_{t-\Delta t}}{\bar{\alpha}_t}}\mathbf{x}_t - \frac{\bar{\alpha}_{t-\Delta t} - \bar{\alpha}_t}{\sqrt{\bar{\alpha}_t\bar{\alpha}_{t-\Delta t}}(1 - \bar{\alpha}_t)}\boldsymbol{\epsilon}_\theta^t(\mathbf{x}_t), \frac{(\bar{\alpha}_{t-\Delta t} - \bar{\alpha}_t)(1 - \bar{\alpha}_{t-\Delta t})}{\bar{\alpha}_{t-\Delta t}(1 - \bar{\alpha}_t)}\mathbf{I}\right.\right),$$

where $\boldsymbol{\epsilon}_\theta^t(\mathbf{x}_t)$ is the estimated denoising gradient from a DDPM from time t to time 0, towards \mathbf{x}_0 from \mathbf{x}_t . For small Δt , this is a good approximation to the diffusion backward process.

JUSTIFICATION. We start with the observation from Luo (2022) that the computation of a sample $\mathbf{x}_{t-\Delta t}$ at time $(t - \Delta t)$, conditioned on \mathbf{x}_t and \mathbf{x}_0 , follows a Gaussian form. This can be seen as follows

$$\begin{aligned} & q(\mathbf{x}_{t-\Delta t}|\mathbf{x}_t, \mathbf{x}_0) \\ &= \frac{q(\mathbf{x}_{t-\Delta t}, \mathbf{x}_t, \mathbf{x}_0)}{q(\mathbf{x}_t, \mathbf{x}_0)} \\ &= \frac{q(\mathbf{x}_t|\mathbf{x}_{t-\Delta t}, \mathbf{x}_0)q(\mathbf{x}_{t-\Delta t}|\mathbf{x}_0)}{q(\mathbf{x}_t|\mathbf{x}_0)} \\ &= \frac{\mathcal{N}\left(\mathbf{x}_t; \sqrt{\bar{\alpha}_t/\bar{\alpha}_{t-\Delta t}}\mathbf{x}_{t-\Delta t}, (1 - \bar{\alpha}_t/\bar{\alpha}_{t-\Delta t})\mathbf{I}\right)\mathcal{N}(\mathbf{x}_{t-\Delta t}; \sqrt{\bar{\alpha}_{t-\Delta t}}\mathbf{x}_0, (1 - \bar{\alpha}_{t-\Delta t})\mathbf{I})}{\mathcal{N}(\mathbf{x}_t; \sqrt{\bar{\alpha}_t}\mathbf{x}_0, (1 - \bar{\alpha}_t)\mathbf{I})} \\ &\propto \exp\left\{-\frac{1}{2}\left[\frac{\left(\mathbf{x}_t - \sqrt{\bar{\alpha}_t/\bar{\alpha}_{t-\Delta t}}\mathbf{x}_{t-\Delta t}\right)^2}{1 - \bar{\alpha}_t/\bar{\alpha}_{t-\Delta t}} + \frac{(\mathbf{x}_{t-\Delta t} - \sqrt{\bar{\alpha}_{t-\Delta t}}\mathbf{x}_0)^2}{1 - \bar{\alpha}_{t-\Delta t}} - \frac{(\mathbf{x}_t - \sqrt{\bar{\alpha}_t}\mathbf{x}_0)^2}{1 - \bar{\alpha}_t}\right]\right\} \\ &\propto \exp\left\{-\frac{1}{2}\left[\left(\frac{\bar{\alpha}_t/\bar{\alpha}_{t-\Delta t}}{1 - \bar{\alpha}_t/\bar{\alpha}_{t-\Delta t}} + \frac{1}{1 - \bar{\alpha}_{t-\Delta t}}\right)\mathbf{x}_{t-\Delta t}^2 - 2\left(\frac{\sqrt{\bar{\alpha}_t/\bar{\alpha}_{t-\Delta t}}}{1 - \bar{\alpha}_t/\bar{\alpha}_{t-\Delta t}}\mathbf{x}_t + \frac{\sqrt{\bar{\alpha}_{t-\Delta t}}}{1 - \bar{\alpha}_{t-\Delta t}}\mathbf{x}_0\right)\mathbf{x}_{t-\Delta t}\right]\right\} \\ &= \exp\left\{-\frac{1}{2}\frac{\bar{\alpha}_{t-\Delta t}(1 - \bar{\alpha}_t)}{(\bar{\alpha}_{t-\Delta t} - \bar{\alpha}_t)(1 - \bar{\alpha}_{t-\Delta t})}\left[\mathbf{x}_{t-\Delta t}^2 - 2\frac{(1 - \bar{\alpha}_{t-\Delta t})\sqrt{\bar{\alpha}_{t-\Delta t}\bar{\alpha}_t}\mathbf{x}_t + (\bar{\alpha}_{t-\Delta t} - \bar{\alpha}_t)\sqrt{\bar{\alpha}_{t-\Delta t}}\mathbf{x}_0}{\bar{\alpha}_{t-\Delta t}(1 - \bar{\alpha}_t)}\mathbf{x}_{t-\Delta t}\right]\right\} \\ &\propto \mathcal{N}\left(\mathbf{x}_{t-\Delta t}; \frac{(1 - \bar{\alpha}_{t-\Delta t})\sqrt{\bar{\alpha}_t}\mathbf{x}_t + (\bar{\alpha}_{t-\Delta t} - \bar{\alpha}_t)\mathbf{x}_0}{\sqrt{\bar{\alpha}_{t-\Delta t}}(1 - \bar{\alpha}_t)}, \frac{(\bar{\alpha}_{t-\Delta t} - \bar{\alpha}_t)(1 - \bar{\alpha}_{t-\Delta t})}{\bar{\alpha}_{t-\Delta t}(1 - \bar{\alpha}_t)}\mathbf{I}\right). \end{aligned} \quad (28)$$

While the forward process (Ho et al., 2020) computes

$$\mathbf{x}_t = \sqrt{\bar{\alpha}_t}\mathbf{x}_0 + \sqrt{1 - \bar{\alpha}_t}\boldsymbol{\epsilon}_t, \quad (29)$$

giving that

$$\mathbf{x}_0 = \frac{1}{\sqrt{\bar{\alpha}_t}}(\mathbf{x}_t - \sqrt{1 - \bar{\alpha}_t}\boldsymbol{\epsilon}_t), \quad (30)$$

the exact \mathbf{x}_0 is infeasible to be computed in the backward process.

However, given a diffusion model $\epsilon_\theta^t(\mathbf{x}_t)$ that can estimate the denoising gradient from \mathbf{x}_t , we have a function for estimating \mathbf{x}_0 , given by

$$f_\theta^t(\mathbf{x}_t) = \frac{1}{\sqrt{\bar{\alpha}_t}}(\mathbf{x}_t - \sqrt{1 - \bar{\alpha}_t}\epsilon_\theta^t(\mathbf{x}_t)) . \quad (31)$$

We can now define a non-Markovian backward process as follows

$$p_\theta(\mathbf{x}_{t-\Delta t}|\mathbf{x}_t) = q(\mathbf{x}_{t-\Delta t}|\mathbf{x}_t, f_\theta^t(\mathbf{x}_t)) . \quad (32)$$

The expanded definition is then obtained by substituting Eq. (31) into Eq. (28).

2 THE RUNGE–KUTTA METHOD FOR DIFFUSION MODELS

We first revisit the Runge–Kutta method (RK4) which solves initial value problems (Runge, 1895; Kutta, 1901; Wikipedia, 2023). Given an initial value problem as $f(\mathbf{x}_t, t) = d\mathbf{x}_t/dt$, where \mathbf{x}_t is associated with time t , the estimation of \mathbf{x}_t at time $(t + \Delta t)$ with step size Δt is computed by

$$\mathbf{x}_{t+\Delta t} = \mathbf{x}_t + \frac{\Delta t}{6} (\mathbf{k}_1 + 2\mathbf{k}_2 + 2\mathbf{k}_3 + \mathbf{k}_4) , \quad (33)$$

where

$$\mathbf{k}_1 = f(\mathbf{x}_t, t) , \quad (34)$$

$$\mathbf{k}_2 = f(\mathbf{x}_t + \frac{\Delta t}{2}\mathbf{k}_1, t + \frac{\Delta t}{2}) , \quad (35)$$

$$\mathbf{k}_3 = f(\mathbf{x}_t + \frac{\Delta t}{2}\mathbf{k}_2, t + \frac{\Delta t}{2}) , \quad (36)$$

$$\mathbf{k}_4 = f(\mathbf{x}_t + \Delta t\mathbf{k}_3, t + \Delta t) . \quad (37)$$

For an initial value \mathbf{x}_0 at time $(t = 0)$, one can estimate \mathbf{x}_T iteratively by using Eq. (33) from $(t = 0)$ to the terminate time $(t = T)$.

For the backward process of a diffusion model, the reverse step can be written as

$$\mathbf{x}_{t-\Delta t} = g(\mathbf{x}_t, \epsilon_{t-\Delta t}, t - \Delta t) , \quad (38)$$

where $g(\cdot)$ refers to the backward step in DDPM (Ho et al., 2020) with Gaussian noises or DDIM (Song et al., 2021) without Gaussian noises and $\epsilon_{t-\Delta t}$ is the reversing gradient from \mathbf{x}_t to $\mathbf{x}_{t-\Delta t}$, denoted as “model prediction”. To apply RK4 to the reverse step, we follow the same rule as Eq. (33) but change the moving step as

$$\epsilon_{t-\Delta t} = \frac{1}{6} (\mathbf{k}_1 + 2\mathbf{k}_2 + 2\mathbf{k}_3 + \mathbf{k}_4) , \quad (39)$$

where

$$\mathbf{k}_1 = f(\mathbf{x}_t, t) , \quad (40)$$

$$\mathbf{k}_2 = f(g(\mathbf{x}_t, \mathbf{k}_1, t - \lfloor \frac{\Delta t}{2} \rfloor), t - \lfloor \frac{\Delta t}{2} \rfloor) , \quad (41)$$

$$\mathbf{k}_3 = f(g(\mathbf{x}_t, \mathbf{k}_2, t - \lfloor \frac{\Delta t}{2} \rfloor), t - \lfloor \frac{\Delta t}{2} \rfloor) , \quad (42)$$

$$\mathbf{k}_4 = f(g(\mathbf{x}_t, \mathbf{k}_3, t - \Delta t), t - \Delta t) , \quad (43)$$

where $\lfloor \cdot \rfloor$ rounds to the smaller integer due to the discretization of the sampling time space. The difference of moving steps between Eq. (39) and Eq. (33) is the multiplication of Δt or $(\Delta t/2)$ to \mathbf{k}_i for $i = \{1, 2, 3, 4\}$. Empirically, applying these multiplications in diffusion sampling leads to strongly unrealistic image generation even with small Δt . We thus hypothesize that the moving steps are already considered in $g(\cdot)$ because of the joint effect of the sampling coefficients in $g(\cdot)$, ϵ_t , $\epsilon_{t-\lfloor \Delta t/2 \rfloor}$, and $\epsilon_{t-\Delta t}$.

REFERENCES

- Alanis-Lobato, G., Mier, P., and Andrade-Navarro, M. A. (2016). Manifold learning and maximum likelihood estimation for hyperbolic network embedding. *Applied Network Science*
- Bellman, R. (1957). Dynamic programming. *Princeton University Press*
- Brown, T. B., Mane, D., Roy, A., Abadi, M., and Gilmer, J. (2017). Adversarial patch. *Conference on Neural Information Processing Systems (NeurIPS)*
- Carlini, N. and Wagner, D. A. (2016). Towards evaluating the robustness of neural networks. *CoRR* abs/1608.04644
- Chaabouni, R., Kharitonov, E., Bouchacourt, D., Dupoux, E., and Baroni, M. (2020). Compositionality and generalization in emergent languages. *arXiv:2004.09124*
- Chang, L., Borenstein, E., Zhang, W., and Geman, S. (2017). Maximum likelihood features for generative image models. *Annals of Applied Statistics*
- Chou, E., Tramer, F., and Pellegrino, G. (2019). SentiNet: Detecting localized universal attacks against deep learning systems. *Deep Learning and Security Workshop (DLSW)*
- Coeurdoux, F., Dobigeon, N., and Chainais, P. (2022). Sliced-Wasserstein normalizing flows: beyond maximum likelihood training. *European Symposium on Artificial Neural Networks (ESANN)*
- Gomtsyan, M., Mokrov, N., Panov, M., and Yanovich, Y. (2019). Geometry-aware maximum likelihood estimation of intrinsic dimension. *Proceedings of Machine Learning Research*
- Grover, A., Dhar, M., and Ermon, S. (2018). Flow-GAN: Combining maximum likelihood and adversarial learning in generative models. *AAAI Conference on Artificial Intelligence (AAAI)*
- Hajri, H., Said, S., and Berthoumieu, Y. (2017). Maximum likelihood estimators on manifolds. *International Conference on Geometric Science of Information*
- Havrylov, S. and Titov, I. (2017). Emergence of language with multi-agent games: Learning to communicate with sequences of symbols. *Conference on Neural Information Processing Systems (NeurIPS)* 30
- He, K., Zhang, X., Ren, S., and Sun, J. (2016). Deep residual learning for image recognition. *IEEE Conference on Computer Vision and Pattern Recognition (CVPR)* , 770–778
- Ho, J., Jain, A., and Abbeel, P. (2020). Denoising diffusion probabilistic models. *Conference on Neural Information Processing Systems (NeurIPS)*
- Hwang, R.-H., Lin, J.-Y., Hsieh, S.-Y., Lin, H.-Y., and Lin, C.-L. (2023). Adversarial patch attacks on deep-learning-based face recognition systems using generative adversarial networks. *Sensors (Basel)*
- Kingma, D. P. and Dhariwal, P. (2018). Glow: Generative flow with invertible 1x1 convolutions. *Conference on Neural Information Processing Systems (NeurIPS)*
- Kingma, D. P. and Welling, M. (2013). Auto-encoding variational bayes. *arXiv:1312.6114*
- Klein, S., Raine, J. A., and Golling, T. (2022). Flows for Flows: Training normalizing flows between arbitrary distributions with maximum likelihood estimation. *arXiv:2211.02487*
- Kubricht, J. R., Santamaria-Pang, A., Devaraj, C., Chowdhury, A., and Tu, P. (2020). Emergent languages from pretrained embeddings characterize latent concepts in dynamic imagery. *International Journal of Semantic Computing*
- Kutta, W. (1901). Beitrag zur naheungsweisen integration totaler differentialgleichungen. *Zeitschrift für Mathematik und Physik*
- LeCun, Y., Bottou, L., Bengio, Y., and Haffner, P. (1998). Gradient-based learning applied to document recognition. *Proceedings of the IEEE*
- Lin, J., Song, C., He, K., Wang, L., and Hopcroft, J. E. (2020). Nesterov accelerated gradient and scale invariance for adversarial attacks. *International Conference on Learning Representations (ICLR)*

- Liu, A., Wang, J., Liu, X., Cao, B., Zhang, C., and Yu, H. (2020). Bias-based universal adversarial patch attack for automatic check-out. *European Conference on Computer Vision (ECCV)*
- Liu, B., Yang, F., Bi, X., Xiao, B., Li, W., and Gao, X. (2022). Detecting generated images by real images. *European Conference on Computer Vision (ECCV)*
- Liu, Z., Luo, P., Wang, X., and Tang, X. (2015). Deep learning face attributes in the wild. *Proceedings of International Conference on Computer Vision (ICCV)*
- Luo, C. (2022). Understanding diffusion models: A unified perspective. *arXiv:2208.11970*
- Madry, A., Makelov, A., Schmidt, L., Tsipras, D., and Vladu, A. (2018). Towards deep learning models resistant to adversarial attacks. *International Conference on Learning Representations (ICLR)*
- Mu, Y., Yao, S., Ding, M., Luo, P., and Gan, C. (2023). EC²: Emergent communication for embodied control. *IEEE Conference on Computer Vision and Pattern Recognition (CVPR)*
- Papamakarios, G., Nalisnick, E., Rezende, D. J., Mohamed, S., and Lakshminarayanan, B. (2021). Normalizing flows for probabilistic modeling and inference. *Journal of Machine Learning Research*
- Pope, P., Zhu, C., Abdelkader, A., Goldblum, M., and Goldstein, T. (2021). The intrinsic dimension of images and its impact on learning. *International Conference on Learning Representations (ICLR)*
- Rezende, D. J. and Mohamed, S. (2016). Variational inference with normalizing flows. *International Conference on Machine Learning (ICML)*
- Runge, C. D. T. (1895). Über die numerische auflosung von differentialgleichungen. *Mathematische Annalen, Springer*
- Santamaria-Pang, A., Kubricht, J., Chowdhury, A., Bhushan, C., and Tu, P. (2020). Towards emergent language symbolic semantic segmentation and model interpretability. *Medical Image Computing and Computer Assisted Intervention (MICCAI)*
- Schroff, F., Kalenichenko, D., and Philbin, J. (2015). Facenet: A unified embedding for face recognition and clustering. *IEEE Conference on Computer Vision and Pattern Recognition (CVPR)* , 815–823
- Song, J., Meng, C., and Ermon, S. (2021). Denoising diffusion implicit models. *International Conference on Learning Representations (ICLR)*
- Tramer, F., Kurakin, A., Papernot, N., Goodfellow, I., Boneh, D., and McDaniel, P. (2017). Ensemble adversarial training: Attacks and defenses. *International Conference on Learning Representations (ICLR)*
- Tucker, M., Li, H., Agrawal, S., Hughes, D., Sycara, K., Lewis, M., et al. (2021). Emergent discrete communication in semantic spaces. *Conference on Neural Information Processing Systems (NeurIPS)*
- Wang, S.-Y., Wang, O., Zhang, R., Owens, A., and Efros, A. A. (2020). CNN-generated images are surprisingly easy to spot... for now. *IEEE Conference on Computer Vision and Pattern Recognition (CVPR)*
- Wikipedia (2023). Runge-Kutta methods. https://en.wikipedia.org/wiki/Runge-Kutta_methods
- Xiang, C., Bhagoji, A. N., Sehwag, V., and Mittal, P. (2021). PatchGuard: A provably robust defense against adversarial patches via small receptive fields and masking. *USENIX Security Symposium 2021*
- Yang, Z., Xu, Z., Zhang, J., Hartley, R., and Tu, P. (2022). Adaptive test-time defense with the manifold hypothesis. *arXiv:2210.14404*